PHYSICAL REVIEW B **108**, L241114 (2023)

Letter

Emergent superconductivity in doped ferroelectric hafnia

Xu Duan
School of Science, Zhejiang University of Science and Technology, Hangzhou, Zhejiang 310023, China
and Key Laboratory for Quantum Materials of Zhejiang Province, Department of Physics, School of Science, Westlake University, Hangzhou, Zhejiang 310024, China

Shi Liu [*]
Key Laboratory for Quantum Materials of Zhejiang Province, Department of Physics, School of Science, Westlake University, Hangzhou, Zhejiang 310024, China
and Institute of Natural Sciences, Westlake Institute for Advanced Study, Hangzhou, Zhejiang 310024, China

(Received 15 September 2023; revised 27 November 2023; accepted 30 November 2023; published 15 December 2023)

Superconductivity and ferroelectricity, representing two distinct forms of ordered states, are typically not found together in the same system, making it even more difficult to create a connection between them. Here, supported by first-principles calculations, we propose that Anderson-Blount's ferroelectriclike metal or, more accurately, a polar metal can manifest in electron-doped polar $Pca2_1$ HfO_2. In this system, polar phonons and consequently the structural asymmetry are not affected by the presence of itinerant electrons. We find that an optical phonon, featuring atomic displacements orthogonal to the ferroelectric polarization direction, is strongly coupled to doped electrons and can acquire a pronounced electron-phonon coupling strength to activate conventional Bardeen-Cooper-Schrieffer superconductivity. The displacements of polar oxygen atoms in $Pca2_1$ HfO_2 create a link between ferroelectricity and superconductivity, enabling a tunable superconducting temperature ranging from approximately 10 to 30 Kelvin. Owing to hafnia's compatibility with silicon, we suggest that the HfO_2-based polar superconductor presents an opportunity to construct high-performing hybrid integrated systems utilizing switchable quantum states.

DOI: 10.1103/PhysRevB.108.L241114

Superconductivity and ferroelectricity, despite their striking differences at the fundamental physics level, converge in a shared trait: the representation of "ordered states" [1]. In superconductivity, the ordered state manifests through the orchestrated movement of coupled electron pairs, known as Cooper pairs, leading to the emergent phenomenon of zero electrical resistance. In contrast, the ordered state of a ferroelectric features the alignment of electric dipoles within the material, yielding a macroscopic polarization that can be manipulated by an external field. This symphony of internal order, i.e., the coordinated electron movement in superconductors and the collective response of electric dipoles in ferroelectrics, defines their distinctive and technologically useful properties [2–5]. However, reconciling these two distinct ordered states within a single material has been challenging because mobile electrons in metallic states tend to strongly screen the dipole-dipole interaction that is considered crucial for the emergence of ferroelectricity [6,7].

A unique material system that concurrently exhibits both superconductivity and ferroelectricity is $Sr_{1-x}Ca_xTiO_{3-\delta}$, in which Ca dopants nudge the quantum paraelectric $SrTiO_3$ towards ferroelectricity, while oxygen vacancies provide electron doping to induce superconductivity [8–10]. The origin of superconductivity in doped $SrTiO_3$ and its interplay with ferroelectricity remain unclear [8,11–19]. Multiple theories have been proposed to unravel this intricate phenomena, with several of them emphasizing the importance of the soft transverse optical mode [11,13,20]. Based on their density functional theory (DFT) investigations of electron-doped ferroelectric $BaTiO_3$, Ma *et al.* reported that the soft polar phonons are strongly modulated by the itinerant electrons [21]. This interaction could amplify the strength of electron-phonon coupling and induce phonon-mediated superconductivity. More recently, evidence of on-off switching of superconductivity via gate voltages was observed in bilayer T_d-$MoTe_2$ [22]. This discovery indicates that these two seemingly incompatible ordered states can indeed interact with each other, opening up opportunities for electrostatic control of quantum phases.

The postulated superconductivity in electron-doped $BaTiO_3$ introduces a design principle for polar superconductors: utilizing a well-established ferroelectric through doping to exploit the strong coupling between soft polar phonons and doped itinerant carriers [21]. However, this strategy presents a fundamental compromise as an increased doping concentration often strongly suppresses the polar state [23]. In this Letter, we demonstrate that it is feasible to realize the Anderson-Blount's weak electron coupling mechanism for "ferroelectriclike metals" [24–26] or, more rigorously speaking, polar metal (as the switchability of such a metallic bulk state could be challenging). Our strategy involves two types of phonons. The polar phonons remain surprisingly unaffected by charge-carrier doping. Meanwhile, other phonons, which are decoupled from the ferroelectricity

---

[*] liushi@westlake.edu.cn

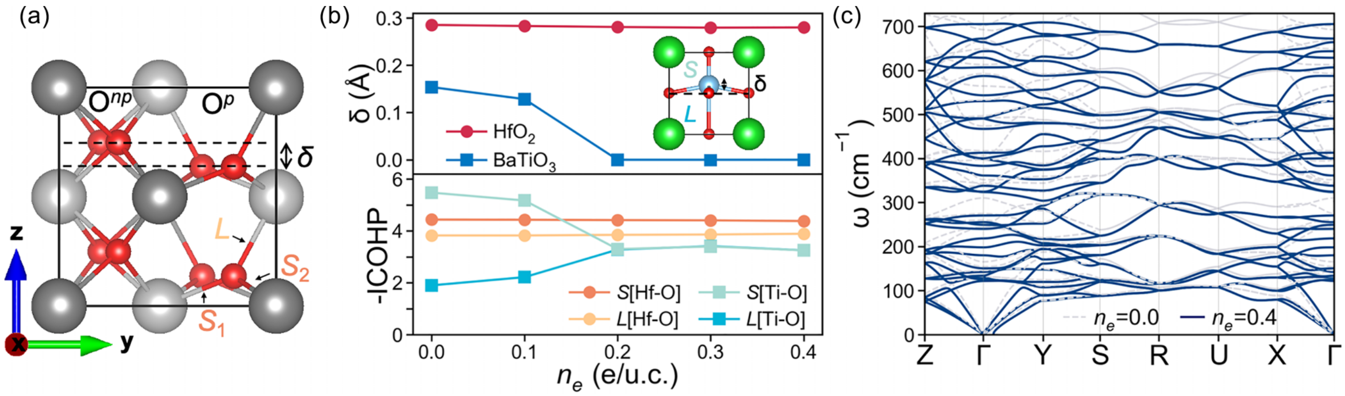

FIG. 1. (a) Crystal structure of ferroelectric $Pca2_1$ HfO$_2$. The displacement (δ) of O^p atoms along the z axis breaks the inversion symmetry. The O^p atoms are coordinated to three Hf atoms, forming three bonds denoted as L, S_1, and S_2, respectively. (b) Polar atomic displacement δ and negative integrated crystal orbital Hamiltonian population ($-$ICOHP) as a function of electron-doping concentration (n_e) for $Pca2_1$ HfO2 and tetragonal BaTiO$_3$. The inset illustrates the polar displacement of Ti in the unit cell of tetragonal BaTiO$_3$. The bottom panel shows the averaged $-$ICOHP value of S_1[Hf-O] and S_2[Hf-O] as S[Hf-O]. (c) Phonon spectra for undoped ($n_e = 0.0$) and electron-doped ($n_e = 0.4$) $Pca2_1$ HfO$_2$.

yet exhibit pronounced electron-phonon coupling, can induce conventional Bardeen-Cooper-Schrieffer (BCS) superconductivity.

The model system we identified is ferroelectric hafnia (HfO$_2$) doped with electrons. Recognized by the industry for their silicon compatibility, HfO$_2$-based ferroelectrics emerge as an outstanding candidate for integrating ferroelectric functionalities into silicon-based circuits [27,28]. In contrast to conventional perovskite ferroelectrics, HfO$_2$-based thin films maintain robust switchable polarization even at nanometer thickness [29–31]. Despite the hotly debated origin of ferroelectricity in hafnia thin films, the polar orthorhombic $Pca2_1$ phase is often identified as the ferroelectric phase [32–35]. The unit cell of $Pca2_1$ HfO$_2$ [Fig. 1(a)] possesses a spacing layer consisting of fourfold-coordinated nonpolar oxygen ions (O^{np}) that separates threefold-coordinated polar oxygen ions (O^p). Previous DFT studies have shown that the $Pca2_1$ phase exhibits an extreme charge-carrier-inert ferroelectricity, where local polar displacements of O^p atoms are insensitive to charge-carrier doping [36]. This unique feature makes doped HfO$_2$ an ideal platform to investigate doping-induced superconductivity with minimal disruption to the polar state.

Here, supported by DFT calculations, we find that electron-doped ferroelectric HfO$_2$ can transition into a BCS superconductor with moderate superconducting transition temperatures (T_c) in the range of tens of Kelvins. Unlike BaTiO$_3$ that experiences an increase in electron-phonon coupling strength due to doping-induced polar mode softening, the enhanced T_c in electron-doped HfO$_2$ primarily stems from the softening of an optical mode that is decoupled from the ferroelectricity. By leveraging the interaction between this optical phonon and the polar displacements of O^p atoms, we demonstrate a tunable T_c ranging from approximately 10 to 30 K. The silicon-compatible polar superconductor proposed here presents opportunities to integrate superconducting devices with existing silicon-based electronics. This could pave the way for scalable hybrid systems with novel functionalities powered by switchable quantum phases.

DFT calculations are carried out using QUANTUM ESPRESSO [37,38] with local density approximation (LDA) [39] and pseudopotentials taken from the Garrity-Bennett-Rabe-Vanderbilt (GBRV) pseudopotential library [40]. The structural parameters of the unit cell of $Pca2_1$ HfO$_2$ are optimized using a plane-wave cutoff of 90 Ry, charge-density cutoff of 720 Ry, $9 \times 9 \times 9$ Γ-centered **k**-point mesh for Brillouin zone (BZ) sampling, energy convergence threshold of 10^{-7} Ry, force convergence threshold of 10^{-6} Ry/Bohr, and stress threshold of 0.5 kBar. The optimized lattice constants are $a = 5.179$ Å, $b = 4.980$ Å, and $c = 4.998$ Å, respectively, which are consistent with the previous report [30]. We note that rather large plane-wave and charge-density cutoffs are employed to achieve convergence in the electronic structure, particularly for the doped systems. Following the protocol in previous studies, the impacts of electrostatic doping are investigated with the background-charge approach with fixed volume in which the number of electrons is adjusted to set the doping concentration, while an additional homogeneous background charge is introduced to ensure charge neutrality [41–43]. For a specific electron-doping concentration (n_e) in the unit of electron per unit cell (e/u.c.), the atomic positions are fully relaxed with lattice constants fixed to undoped ground-state values, followed by a single-point energy calculation using a tighter threshold for self-consistency (10^{-12} Ry). The phonon spectrum is calculated with the density functional perturbation theory using a $3 \times 3 \times 3$ **q**-point mesh. Maximally localized Wannier functions (MLWFs) along with the Migdal-Eliashberg theory implemented in WANNIER90 [44,45] and EPW [46,47] are used to quantify the electron-phonon coupling strength. To begin, the electron-phonon matrix elements are computed using a $6 \times 6 \times 6$ **k**-point mesh in the electron BZ and a $3 \times 3 \times 3$ **q**-point mesh in the phonon BZ. These elements are subsequently interpolated onto finer grids ($18 \times 18 \times 18$ for **k** and **q** points) using MLWFs. The chemical bonding situations in electron-doped HfO$_2$ are analyzed with the integrated crystal orbital Hamilton population (ICOHP) method implemented in LOBSTER [48,49]. All structural files and some representative

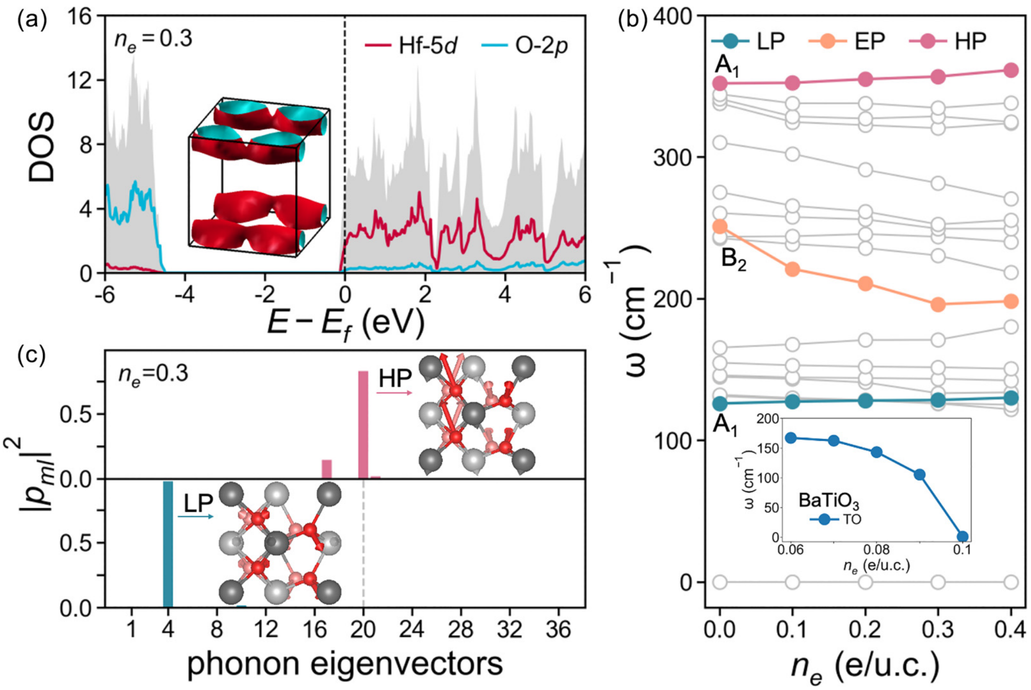

FIG. 2. (a) Projected density of states (DOS) of electron-doped $Pca2_1$ HfO$_2$ at $n_e = 0.3$. The inset shows the Fermi surface. (b) Γ-point phonon frequencies as a function of n_e. Blue and red filled circles highlight two polar optical phonons, LP and HP, respectively. The irreducible representations of the LP, EP, and HP modes are A$_1$, B$_2$, and A$_1$. The doping-induced softening of a zone-center polar transverse optical (TO) mode in tetragonal BaTiO$_3$ is depicted in the inset. (c) Projection coefficients $|p_{ml}|^2$ for HP (top) and LP (bottom) at $n_e = 0.3$ using phonon eigenvectors of undoped HfO$_2$ as the basis set. Insets show the eigenvectors of undoped HP and LP.

input files for DFT calculations are uploaded to a public repository.

The spontaneous polarization in $Pca2_1$ HfO$_2$ results from the atomic displacements (δ) of O^p atoms relative to the center of neighboring Hf planes along the z axis [Fig. 1(a)]. Figure 1(b) illustrates the value of δ as a function of n_e, together with the results for BaTiO$_3$ included for comparison. Consistent with previous DFT studies [21,41], electron doping drastically suppresses the polar displacements of Ti atoms in BaTiO$_3$, but induces a negligible impact on the magnitude of δ in $Pca2_1$ HfO$_2$. We further compute ICOHPs for the three Hf-O^p bonds and find that they preserve nearly constant bonding strengths, showing no significant sensitivity to increased electron doping [Fig. 1(b), bottom panel]. This behavior contrasts with that observed in BaTiO$_3$: electron doping weakens the shorter Ti-O bond while strengthening the longer Ti-O bond along the polar axis, consequently diminishing the extent of inversion symmetry breaking. Additionally, a high doping concentration of $n_e = 0.4$ does not compromise the dynamical stability of $Pca2_1$ HfO$_2$, as confirmed by the corresponding phonon spectrum that exhibits no imaginary frequencies along the high-symmetry lines of the BZ [Fig. 1(c)].

The origin of the extreme charge-carrier-inert polar structure in $Pca2_1$ HfO$_2$ is elusive. In its pristine state, ferroelectric HfO$_2$ is an insulator with a LDA band gap of approximately 4.32 eV. Upon adding electrons, the Fermi level rises through the conduction band, transforming the system into a doped metal. The projected density of state (DOS) analysis indicates that the added electrons will predominantly occupy Hf-5*d* orbitals [Fig. 2(a)]. Comparatively, in electron-doped BaTiO$_3$, the added electrons will mostly be accommodated in Ti-3*d* orbitals, causing Ti cations to deviate from the formally d^0 electron configuration and reducing the second-order Jahn-Teller (SOJT) activity responsible for spontaneous symmetry breaking [41,50]. In the case of $Pca2_1$ HfO$_2$, the inversion symmetry breaking has been ascribed to a trilinear coupling of three modes, similar to that in hybrid improper ferroelectrics [51]. We also acknowledge a recent DFT study that revealed the proper ferroelectric nature of HfO$_2$ with the *Pbcn* phase as the nonpolar reference phase [52]. Structurally, the polarization of HfO$_2$ originates from the displacements of anions rather than cations as in BaTiO$_3$. Therefore, it is plausible to hypothesize that the ferroelectricity in $Pca2_1$ does not involve SOJT of Hf cations and is less affected by electron doping. This is also confirmed by the weak n_e dependence of the barrier height that separates two opposite polar states of $Pca2_1$ HfO$_2$ (see Supplemental Material [53]).

To gain a microscopic understanding of the doping effect, we calculate the phonon frequencies at the Γ point as a function of n_e. The results for modes with frequencies below 380 cm^{-1} are illustrated in Fig. 2(b). As electron doping can affect mode frequencies and potentially induce mode mixing, establishing a correlation between modes at different doping concentrations can be difficult. We use the mode-projection method [54,55] to track the evolution of a phonon mode with varying n_e. At the BZ center, since the phonon eigenvectors at one doping concentration n_{e1} serve as a complete basis set, they can be applied to expand the phonon eigenvectors at anther doping concentration n_{e2} as

$$\left|\epsilon_l^{i\alpha}(n_{e2})\right\rangle = \sum_m p_{ml}\left|\epsilon_m^{i\alpha}(n_{e1})\right\rangle. \tag{1}$$

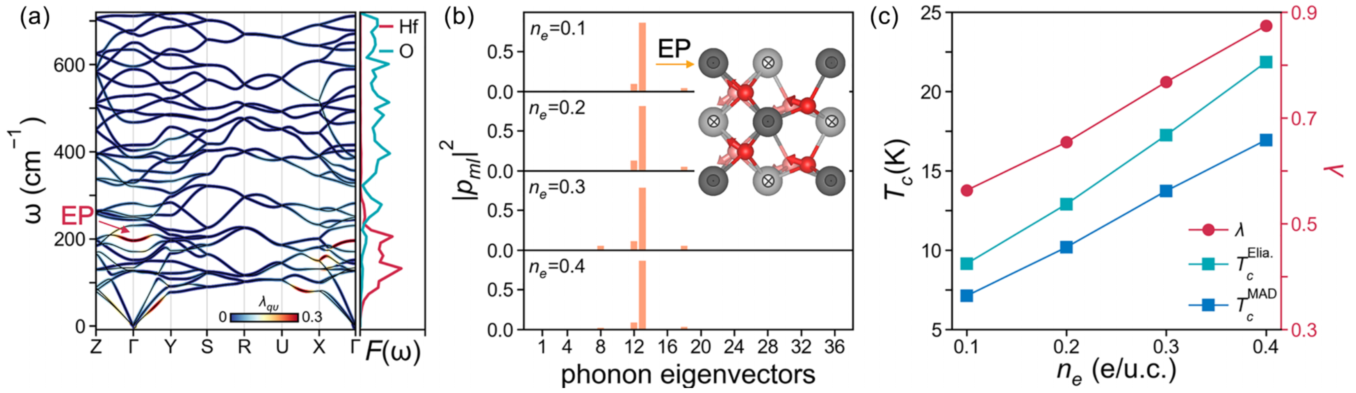

FIG. 3. (a) $\lambda_{\mathbf{q}\nu}$-resolved phonon spectrum and projected phonon DOS of doped HfO$_2$ at $n_e = 0.3$. The Γ-point mode with the highest electron-phonon coupling strength is denoted as EP. (b) Projection coefficients for EP at different doping concentrations. The inset shows the atomic vibrations of undoped EP. Projections to other planes are presented in the Supplemental Material [53]. (c) Superconducting transition temperature T_c computed with two different methods (T_c^{MAD} and $T_c^{\mathrm{Elia.}}$) and total electron-phonon coupling constant λ as a function of n_e. $\mu^* = 0.1$ is used to estimate T_c.

Here, $|\epsilon_l^{i\alpha}(n_{e1})\rangle$ and $|\epsilon_m^{i\alpha}(n_{e2})\rangle$ represent the phonon eigenvectors at doping concentrations n_{e1} and n_{e2}, respectively; m and l are mode indices, i is the atom index, and α specifies the direction (x, y, z). The mode-projection coefficient p_{ml}, characterizing the correlation between mode m and mode l, is given as

$$p_{ml} = \sum_{i\alpha} \left\langle \epsilon_m^{i\alpha}(n_{e1}) \middle| \epsilon_l^{i\alpha}(n_{e2}) \right\rangle. \tag{2}$$

Based on the values of p_{ml}, we relate the phonon modes between two neighboring n_e, as represented by the solid lines in Fig. 2(b).

We first discuss the electron-doping effect on two flat polar phonon modes in $Pca2_1$ HfO$_2$ identified in previous studies [30]. The low-frequency polar mode (denoted as LP) involves atomic displacements of all the modes that undergo condensation during the cubic-to-orthorhombic transition, while the high-frequency polar mode (referred to as HP) involves polar and antipolar displacements of oxygen atoms. Figure 2(c) displays the projection coefficients $|p_{ml}|^2$ for LP and HP at $n_e = 0.3$, using the phonon eigenvectors of undoped HfO$_2$ as the basis set. In the undoped HfO$_2$, LP corresponds to the lowest-frequency optical model ($m = 4$). At $n_e = 0.3$, LP is characterized by $l = 6$ and $|p_{m=4,l}|^2 = 0.9$. This means that despite the reordering of modes based on frequencies after doping, the phonon eigenvector of LP largely retains its original undoped form. In comparison, the doped HP is identified by $l = 20$ and is derived from two undoped modes, i.e., 15% from a mode with $m = 17$ and 85% from the original HP ($m = 20$). Overall, electron doping does not cause substantial mode mixing for the two polar modes in HfO$_2$. This markedly differs from perovskite ferroelectrics, where the mode mixing caused by metallicity is a fairly universal phenomenon and occurs in many systems such as BaTiO$_3$, PbTiO$_3$ [54], and LaSrMnO$_3$/LaNiO$_3$ [56]. Another feature of HfO$_2$ that is distinct from BaTiO$_3$ is the doping-induced hardening of polar modes: the frequency of LP (HP) depends on n_e linearly with a positive slop ($\Delta\omega/\Delta n_e$) of 10.3 cm^{-1} (23.4 cm^{-1}), as shown in Fig. 2(b). These results suggest that electron-doped $Pca2_1$ HfO$_2$ qualifies as an extrinsic polar metal supporting Anderson-Blount's weak electron coupling mechanism: polar modes, primarily involving vibrations of O atoms, are weakly coupled to itinerant electrons located on Hf atoms. A similar weak coupling feature likely presents in polar metals such as LiOsO$_3$, where the free carriers are situated on Os and O atoms, while the Li atoms contribute to most polar distortions [25].

We now focus on the electron-phonon coupling in electron-doped $Pca2_1$ HfO$_2$. Figure 3(a) presents the mode-resolved electron-phonon coupling strength $\lambda_{\mathbf{q}\nu}$ for each individual phonon mode (indexed by $\mathbf{q}$ and band ν) at $n_e = 0.3$. Interestingly, the Γ-point phonon mode (denoted as EP) with the most significant electron-phonon coupling strength is an optical mode characterized by atomic displacements orthogonal to the ferroelectric polarization direction. This feature again is distinct from that of electron-doped BaTiO$_3$, where the zone-center polar mode exhibits the greatest electron-phonon coupling strength [21]. The projected phonon density of states (DOS) $F(\omega)$ [Fig. 3(a)] reveals that the phonon modes with frequencies under ≈200 cm^{-1} are predominantly governed by the vibrations of Hf atoms due to their larger atomic mass compared to O atoms. Additionally, acoustic phonon bands along Γ-Y and U-X paths as well as the optical phonon bands along the Γ-X path have considerable magnitudes of $\lambda_{\mathbf{q}\nu}$.

The frequency of EP as a function of n_e is displayed in Fig. 2(b), with the evolution determined using the mode-projection method, showing a notable mode softening with $\Delta\omega/\Delta n_e = -132$ cm^{-1}. Moreover, the phonon eigenvector of EP remains nearly invariant with respect to n_e. The projection coefficients of EP as a function of n_e [Fig. 3(b)] indicate that this mode mainly originates from the optical mode of $m = 13$ in undoped HfO$_2$, involving vibrations of both Hf and O atoms at roughly equivalent amplitudes [see inset of Fig. 3(b)]. This could explain the large electron-phonon coupling strength of EP: both the doped itinerant electrons and lattice vibrations are associated with Hf atoms.

The softening of EP induced by electron doping further enhances its electron-phonon coupling strength as $\lambda_{\mathbf{q}\nu} \propto \omega_{\mathbf{q}\nu}^{-2}$. The Eliashberg spectral function $\alpha^2F(\omega)$ and accumulative electron-phonon coupling $\lambda(\omega)$ of doped HfO$_2$ are provided

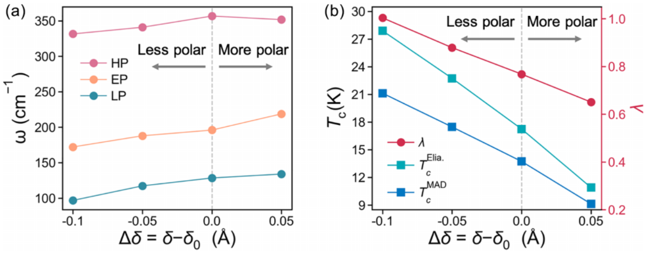

FIG. 4. (a) Frequencies of HP, EP, and LP modes at the Γ point as a function of $\Delta\delta$ that measures the degree of inversion symmetry breaking. The doping concentration is $n_e = 0.3$. (b) Superconducting transition temperature T_c and total electron-phonon coupling constant λ as a function $\Delta\delta$.

in the Supplemental Material [53]. The total electron-phonon coupling constant λ at $n_e = 0.3$ is 0.77, which is sufficiently large to induce phonon-mediated superconductivity [21,57,58]. The transition temperature T_c is estimated with two methods, i.e., the McMillan-Allen-Dynes formula (T_c^{MAD}) [59] and the solution of the Migdal-Eliashberg equations ($T_c^{\mathrm{Elia.}}$) [46,60]. As shown in Fig. 3(c), both T_c^{MAD} and $T_c^{\mathrm{Elia.}}$ elevate with increasing n_e. It is well known that the magnitude of T_c is sensitive to the value of Coulomb pseudopotential μ^* [61,62]. Our test suggests that T_c decreases from 31 to 4 K as μ^* varies from 0 to 0.3 at $n_e = 0.3$ (see Supplemental Material [53]). While the precise value of superconducting T_c is subject to the uncertainty of μ^* and other parameter specifics, we believe that the enhancement of T_c as n_e increases, arising from the EP mode softening, is a robust outcome. A conservative predication for $n_e = 0.3$ using $\mu^* = 0.1$ is that ferroelectric HfO_2 transitions into a superconducting state when the temperature drops below ≈17 K.

Although the polar phonons (HP and LP) are not responsible for the emergence of superconductivity in electron-doped $Pca2_1$ HfO_2, we suggest a tunable T_c could still be achieved by modulating the polar displacements of O^p atoms, potentially enabling field-regulable quantum phases. The interplay between structural asymmetry and superconductivity arises from the fact that the displacement vector of O^p atoms along the polar axis, tunable by external stimuli such as epitaxial strain [63,64], is not orthogonal to the eigenvector of EP. We perform a series of model calculations to quantify the relationship between T_c and δ at a representative doping concentration ($n_e = 0.3$). More specifically, we manually alter the positions of the O^p atoms; the change in the degree of inversion symmetry breaking is measured as $\Delta\delta = \delta - \delta_0$, where δ_0 represents the O^p displacement at the ground state and a negative value of $\Delta\delta$ signifies reduced asymmetry. The relationship between $\Delta\delta$ and the frequency for the LP, HP, and EP modes is depicted in Fig. 4(a), revealing a positive correlation between ω and $\Delta\delta$. Consequently, pushing the structure to a less polar state will soften the EP mode, increase the electron-phonon coupling strength, and raise the T_c [Fig. 4(b)]. By adjusting the positions of the O^p atoms within a range of ±0.1 Å from their equilibrium values, it is possible to accomplish a shift in the superconducting temperature by a factor of two.

In summary, electron-doped $Pca2_1$ HfO_2 is identified as an Anderson-Blount's extrinsic polar metal, where the polar phonon modes exhibit rather limited sensitivity to itinerant electrons. The emerging extreme charge-carrier-inert structural asymmetry provides a foundation for developing polar superconductors. An optical phonon that undergoes softening due to electron doping attains a sufficiently large electron-phonon coupling strength, thereby enabling BCS superconductivity. Notably, with an appropriate doping concentration, the superconducting T_c of ferroelectric HfO_2 could surpass those of doped perovskite ferroelectrics (≈2 K) [21] and most superconducting binary oxides such as LaO (≈5 K) [57], RuO_2 (≈1.7 K) [65,66], NbO_x (≈1.38 K), TiO_x (≈1 K) [67], and SnO (≈1.4 K) [68]. The distinct origins of spontaneous inversion symmetry breaking and superconductivity do not exclude their potential to interact, as the polar displacements of oxygen atoms involve both polar phonons that govern structural distortions and EP phonons that mediate the binding of electrons. The prospect of a tunable T_c over a window of at least 10 K, which is achievable by modulating polar distortions, presents exciting opportunities. We hope this work will stimulate experiments to explore superconductivity in electron-doped HfO_2 and to facilitate the design and discovery of silicon-compatible polar superconductors for novel device applications. A genuine ferroelectric superconductor is possible if the polar state can be switched by external fields, such as electric fields in ultrathin films with thickness comparable to two-dimensional (2D) materials [22] or a strain gradient [69].

X.D. and S.L. acknowledge the support from the National Key R&D Program of China (Grant No. 2021YFA1202100), National Natural Science Foundation of China (Grant No. 12074319), and Westlake Education Foundation. The computational resource is provided by the Westlake HPC Center.

---

[1] H. Y. Hwang, Y. Iwasa, M. Kawasaki, B. Keimer, N. Nagaosa, and Y. Tokura, Emergent phenomena at oxide interfaces, Nat. Mater. **11**, 103 (2012).

[2] R. Dalven, Superconductive devices and materials, in *Introduction to Applied Solid State Physics: Topics in the Applications of Semiconductors, Superconductors, and the Nonlinear Optical Properties of Solids* (Springer US, Boston, MA, 1980), pp. 215–255.

[3] I. Holzman and Y. Ivry, Superconducting nanowires for single-photon detection: Progress, challenges, and opportunities, Adv. Quantum Technol. **2**, 1800058 (2019).

[4] J. F. Scott, Applications of modern ferroelectrics, Science **315**, 954 (2007).

[5] H. J. Zhao, A. Filippetti, C. Escorihuela-Sayalero, P. Delugas, E. Canadell, L. Bellaiche, V. Fiorentini, and J. Íñiguez, Meta-screening and permanence of polar distortion in metallized ferroelectrics, Phys. Rev. B **97**, 054107 (2018).

[6] R. E. Cohen, Origin of ferroelectricity in perovskite oxides, Nature (London) **358**, 136 (1992).

[7] H. J. Xiang, Origin of polar distortion in $LiNbO_3$-type "ferroelectric" metals: Role of A-site instability and short-range interactions, Phys. Rev. B **90**, 094108 (2014).

[8] C. W. Rischau, X. Lin, C. P. Grams, D. Finck, S. Harms, J. Engelmayer, T. Lorenz, Y. Gallais, B. Fauqué, J. Hemberger, and K. Behnia, A ferroelectric quantum phase transition inside the superconducting dome of $Sr_{1-x}Ca_xTiO_{3-\delta}$, Nat. Phys. **13**, 643 (2017).

[9] J. G. Bednorz and K. A. Müller, $Sr_{1-x}Ca_xTiO_3$: An XY quantum ferroelectric with transition to randomness, Phys. Rev. Lett. **52**, 2289 (1984).

[10] J. Wang, L. Yang, C. W. Rischau, Z. Xu, Z. Ren, T. Lorenz, J. Hemberger, X. Lin, and K. Behnia, Charge transport in a polar metal, npj Quantum Mater. **4**, 61 (2019).

[11] J. M. Edge, Y. Kedem, U. Aschauer, N. A. Spaldin, and A. V. Balatsky, Quantum critical origin of the superconducting dome in $SrTiO_3$, Phys. Rev. Lett. **115**, 247002 (2015).

[12] Y. Kedem, J. X. Zhu, and A. V. Balatsky, Unusual superconducting isotope effect in the presence of a quantum criticality, Phys. Rev. B **93**, 184507 (2016).

[13] D. van der Marel, F. Barantani, and C. W. Rischau, Possible mechanism for superconductivity in doped $SrTiO_3$, Phys. Rev. Res. **1**, 013003 (2019).

[14] S. Kanasugi and Y. Yanase, Multiorbital ferroelectric superconductivity in doped $SrTiO_3$, Phys. Rev. B **100**, 094504 (2019).

[15] A. P. Baratoff and G. K. Binnig, Mechanism of superconductivity in $SrTiO_3$, Physica B+C **108**, 1335 (1981).

[16] A. G. Swartz, H. Inoue, T. A. Merz, Y. Hikita, S. Raghu, T. P. Devereaux, S. Johnston, and H. Y. Hwang, Polaronic behavior in a weak-coupling superconductor, Proc. Natl. Acad. Sci. USA **115**, 1475 (2018).

[17] Y. Tomioka, N. Shirakawa, K. Shibuya, and I. H. Inoue, Enhanced superconductivity close to a nonmagnetic quantum critical point in electron-doped strontium titanate, Nat. Commun. **10**, 738 (2019).

[18] C. Enderlein, J. F. de Oliveira, D. A. Tompsett, E. B. Saitovitch, S. S. Saxena, G. G. Lonzarich, and S. E. Rowley, Superconductivity mediated by polar modes in ferroelectric metals, Nat. Commun. **11**, 4852 (2020).

[19] J. Ruhman and P. A. Lee, Superconductivity at very low density: The case of strontium titanate, Phys. Rev. B **94**, 224515 (2016).

[20] P. Wölfle and A. V. Balatsky, Superconductivity at low density near a ferroelectric quantum critical point: Doped $SrTiO_3$, Phys. Rev. B **98**, 104505 (2018).

[21] J. Ma, R. Yang, and H. Chen, A large modulation of electron-phonon coupling and an emergent superconducting dome in doped strong ferroelectrics, Nat. Commun. **12**, 2314 (2021).

[22] A. Jindal, A. Saha, Z. Li, T. Taniguchi, K. Watanabe, J. C. Hone, T. Birol, R. M. Fernandes, C. R. Dean, A. N. Pasupathy, and D. A. Rhodes, Coupled ferroelectricity and superconductivity in bilayer T_d-$MoTe_2$, Nature (London) **613**, 48 (2023).

[23] X. hui Yang, W. hua Hu, J. lu Wang, Z. kai Xu, T. Wang, Z. feng Lou, and X. Lin, A doping threshold for polar metals, npj Quantum Mater. **8**, 47 (2023).

[24] P. W. Anderson and E. I. Blount, Symmetry considerations on martensitic transformations: "Ferroelectric" metals? Phys. Rev. Lett. **14**, 217 (1965).

[25] N. J. Laurita, A. Ron, J. Y. Shan, D. Puggioni, N. Z. Koocher, K. Yamaura, Y. Shi, J. M. Rondinelli, and D. Hsieh, Evidence for the weakly coupled electron mechanism in an Anderson-Blount polar metal, Nat. Commun. **10**, 3217 (2019).

[26] D. Puggioni and J. M. Rondinelli, Designing a robustly metallic noncentrosymmetric ruthenate oxide with large thermopower anisotropy, Nat. Commun. **5**, 3432 (2014).

[27] T. S. Böscke, J. Müller, D. Bräuhaus, U. Schröder, and U. Böttger, Ferroelectricity in hafnium oxide thin films, Appl. Phys. Lett. **99**, 102903 (2011).

[28] M.-K. Kim, I.-J. Kim, and J.-S. Lee, CMOS-compatible ferroelectric NAND flash memory for high-density, low-power, and high-speed three-dimensional memory, Sci. Adv. **7**, eabe1341 (2021).

[29] A. Chernikova, M. Kozodaev, A. Markeev, D. Negrov, M. Spiridonov, S. Zarubin, O. Bak, P. Buragohain, H. Lu, E. Suvorova, A. Gruverman, and A. Zenkevich, Ultrathin $Hf_{0.5}Zr_{0.5}O_2$ ferroelectric films on Si, ACS Appl. Mater. Interfaces **8**, 7232 (2016).

[30] H.-J. Lee, M. Lee, K. Lee, J. Jo, H. Yang, Y. Kim, S. C. Chae, U. Waghmare, and J. H. Lee, Scale-free ferroelectricity induced by flat phonon bands in HfO_2, Science **369**, 1343 (2020).

[31] S. S. Cheema, D. Kwon, N. Shanker, R. dos Reis, S.-L. Hsu, J. Xiao, H. Zhang, R. Wagner, A. Datar, M. R. McCarter, C. R. Serrao, A. K. Yadav, G. Karbasian, C.-H. Hsu, A. J. Tan, L.-C. Wang, V. Thakare, X. Zhang, A. Mehta, E. Karapetrova *et al.*, Enhanced ferroelectricity in ultrathin films grown directly on silicon, Nature (London) **580**, 478 (2020).

[32] M. H. Park, Y. H. Lee, H. J. Kim, Y. J. Kim, T. Moon, K. D. Kim, J. Müller, A. Kersch, U. Schroeder, T. Mikolajick, and C. S. Hwang, Ferroelectricity and antiferroelectricity of doped thin HfO_2-based films, Adv. Mater. **27**, 1811 (2015).

[33] T. D. Huan, V. Sharma, G. A. Rossetti, and R. Ramprasad, Pathways towards ferroelectricity in hafnia, Phys. Rev. B **90**, 064111 (2014).

[34] X. Sang, E. D. Grimley, T. Schenk, U. Schroeder, and J. M. LeBeau, On the structural origins of ferroelectricity in HfO_2 thin films, Appl. Phys. Lett. **106**, 162905 (2015).

[35] R. Materlik, C. Künneth, and A. Kersch, The origin of ferroelectricity in $Hf_{1-x}Zr_xO_2$: A computational investigation and a surface energy model, J. Appl. Phys. **117**, 134109 (2015).

[36] L.-Y. Ma and S. Liu, Structural polymorphism kinetics promoted by charged oxygen vacancies in HfO_2, Phys. Rev. Lett. **130**, 096801 (2023).

[37] P. Giannozzi, S. Baroni, N. Bonini, M. Calandra, R. Car, C. Cavazzoni, D. Ceresoli, G. L. Chiarotti, M. Cococcioni, I. Dabo *et al.*, QUANTUM ESPRESSO: A modular and open-source software project for quantum simulations of materials, J. Phys.: Condens. Matter **21**, 395502 (2009).

[38] P. Giannozzi Jr, O. Andreussi, T. Brumme, O. Bunau, M. B. Nardelli, M. Calandra, R. Car, C. Cavazzoni, D. Ceresoli, M. Cococcioni *et al.*, Advanced capabilities for materials modelling with QUANTUM ESPRESSO, J. Phys.: Condens. Matter **29**, 465901 (2017).

[39] J. P. Perdew and A. Zunger, Self-interaction correction to density-functional approximations for many-electron systems, Phys. Rev. B **23**, 5048 (1981).

[40] K. F. Garrity, J. W. Bennett, K. M. Rabe, and D. Vanderbilt, Pseudopotentials for high-throughput DFT calculations, Comput. Mater. Sci. **81**, 446 (2014).

[41] V. F. Michel, T. Esswein, and N. A. Spaldin, Interplay between ferroelectricity and metallicity in $BaTiO_3$, J. Mater. Chem. C **9**, 8640 (2021).

[42] F. Bruneval, C. Varvenne, J.-P. Crocombette, and E. Clouet, Pressure, relaxation volume, and elastic interactions in charged simulation cells, Phys. Rev. B **91**, 024107 (2015).

[43] D. Hickox-Young, D. Puggioni, and J. M. Rondinelli, Polar metals taxonomy for materials classification and discovery, Phys. Rev. Mater. **7**, 010301 (2023).

[44] N. Marzari, A. A. Mostofi, J. R. Yates, I. Souza, and D. Vanderbilt, Maximally localized Wannier functions: Theory and applications, Rev. Mod. Phys. **84**, 1419 (2012).

[45] G. Pizzi, V. Vitale, R. Arita, S. Blügel, F. Freimuth, G. Géranton, M. Gibertini, D. Gresch, C. Johnson, T. Koretsune, J. Ibañez-Azpiroz, H. Lee, J.-M. Lihm, D. Marchand, A. Marrazzo, Y. Mokrousov, J. I. Mustafa, Y. Nohara, Y. Nomura, L. Paulatto *et al.*, WANNIER90 as a community code: New features and applications, J. Phys.: Condens. Matter **32**, 165902 (2020).

[46] S. Poncé, E. Margine, C. Verdi, and F. Giustino, EPW: Electron-phonon coupling, transport and superconducting properties using maximally localized Wannier functions, Comput. Phys. Commun. **209**, 116 (2016).

[47] F. Giustino, M. L. Cohen, and S. G. Louie, Electron-phonon interaction using Wannier functions, Phys. Rev. B **76**, 165108 (2007).

[48] R. Dronskowski and P. E. Bloechl, Crystal orbital Hamilton populations (COHP): Energy-resolved visualization of chemical bonding in solids based on density-functional calculations, J. Phys. Chem. **97**, 8617 (1993).

[49] S. Maintz, V. Deringer, A. Tchougréeff, and R. Dronskowski, LOBSTER: A tool to extract chemical bonding from plane-wave based DFT, J. Comput. Chem. **37**, 1030 (2016).

[50] D. Hickox-Young, D. Puggioni, and J. M. Rondinelli, Persistent polar distortions from covalent interactions in doped $BaTiO_3$, Phys. Rev. B **102**, 014108 (2020).

[51] F. Delodovici, P. Barone, and S. Picozzi, Trilinear-coupling-driven ferroelectricity in HfO_2, Phys. Rev. Mater. **5**, 064405 (2021).

[52] A. Raeliarijaona and R. E. Cohen, Hafnia HfO_2 is a proper ferroelectric, Phys. Rev. B **108**, 094109 (2023).

[53] See Supplemental Material at http://link.aps.org/supplemental/10.1103/PhysRevB.108.L241114 for additional results including switching barriers, Eliashberg spectral function, superconducting temperature, and mode analysis.

[54] Z. Yimer and H. Fu, Origin of the persistence of soft modes in metallic ferroelectrics, Phys. Rev. B **101**, 174105 (2020).

[55] A. Raeliarijaona and H. Fu, Mode sequence, frequency change of nonsoft phonons, and LO-TO splitting in strained tetragonal $BaTiO_3$, Phys. Rev. B **92**, 094303 (2015).

[56] S. Ghosh, A. Y. Borisevich, and S. T. Pantelides, Engineering an insulating ferroelectric superlattice with a tunable band gap from metallic components, Phys. Rev. Lett. **119**, 177603 (2017).

[57] P.-H. Sun, J.-F. Zhang, K. Liu, Q. Han, and Z.-Y. Lu, First-principles study of the superconductivity in LaO, Phys. Rev. B **104**, 045121 (2021).

[58] R.-Y. Zhao, X.-W. Yan, and M. Gao, Inverted V-shaped evolution of superconducting temperature in SrBC under pressure, Chin. Phys. B **30**, 076301 (2021).

[59] P. B. Allen and R. C. Dynes, Transition temperature of strong-coupled superconductors reanalyzed, Phys. Rev. B **12**, 905 (1975).

[60] E. R. Margine and F. Giustino, Anisotropic Migdal-Eliashberg theory using Wannier functions, Phys. Rev. B **87**, 024505 (2013).

[61] C. F. Richardson and N. W. Ashcroft, High temperature superconductivity in metallic hydrogen: Electron-electron enhancements, Phys. Rev. Lett. **78**, 118 (1997).

[62] K.-H. Lee, K. J. Chang, and M. L. Cohen, First-principles calculations of the Coulomb pseudopotential μ^*: Application to Al, Phys. Rev. B **52**, 1425 (1995).

[63] C. Herrera, J. Cerbin, A. Jayakody, K. Dunnett, A. V. Balatsky, and I. Sochnikov, Strain-engineered interaction of quantum polar and superconducting phases, Phys. Rev. Mater. **3**, 124801 (2019).

[64] K. Ahadi, L. Galletti, Y. Li, S. Salmani-Rezaie, W. Wu, and S. Stemmer, Enhancing superconductivity in $SrTiO_3$ films with strain, Sci. Adv. **5**, eaaw0120 (2019).

[65] J. P. Ruf, H. Paik, N. J. Schreiber, H. P. Nair, L. Miao, J. K. Kawasaki, J. N. Nelson, B. D. Faeth, Y. Lee, B. H. Goodge, B. Pamuk, C. J. Fennie, L. F. Kourkoutis, D. G. Schlom, and K. M. Shen, Strain-stabilized superconductivity, Nat. Commun. **12**, 59 (2021).

[66] M. Uchida, T. Nomoto, M. Musashi, R. Arita, and M. Kawasaki, Superconductivity in uniquely strained RuO_2 films, Phys. Rev. Lett. **125**, 147001 (2020).

[67] J. K. Hulm, C. K. Jones, R. A. Hein, and J. W. Gibson, Superconductivity in the TiO and NbO systems, J. Low Temp. Phys. **7**, 291 (1972).

[68] M. K. Forthaus, K. Sengupta, O. Heyer, N. E. Christensen, A. Svane, K. Syassen, D. I. Khomskii, T. Lorenz, and M. M. Abd-Elmeguid, Superconductivity in SnO: A nonmagnetic analog to Fe-based superconductors? Phys. Rev. Lett. **105**, 157001 (2010).

[69] A. Zabalo and M. Stengel, Switching a polar metal via strain gradients, Phys. Rev. Lett. **126**, 127601 (2021).